Structural, Electronic, and Magnetic Properties of Gd–Substituted Bi2Fe4O9 Multiferroic: A Combined Experimental and DFT Approach

6 authors, including:

Soumyaranjan Mohapatra
KIIT University
51 PUBLICATIONS **404** CITATIONS

Abhipsa Pati
KIIT University
1 PUBLICATION **0** CITATIONS

Lokanath Patra
Georgia Institute of Technology
61 PUBLICATIONS **279** CITATIONS

Jnanranjan Panda
Sri Sri University
14 PUBLICATIONS **316** CITATIONS

Structural, Electronic, and Magnetic Properties of Gd-Substituted Bi$_2$Fe$_4$O$_9$ Multiferroic: A Combined Experimental and DFT Approach

S. R. Mohapatra,[1,z] Lokanath Patra,[2] Abhipsa Pati,[1] A. K. Singh,[3] Jnanranjan Panda,[4] and Hari S. Mohanty[5]

[1]*School of Applied Sciences, Kalinga Institute of Industrial Technology University, Bhubaneswar 751024, India*
[2]*Department of Mechanical Engineering, University of California, Santa Barbara, California 93106, United States of America*
[3]*Department of Physics and Astronomy, National Institute of Technology Rourkela, Rourkela-769008, India*
[4]*Faculty of Science, Sri Sri University, Cuttack 754006, India*
[5]*Department of Physics, Gandhi Institute of Engineering and Technology University, Gunupur 765022, India*

We present the structural, electronic, and magnetic properties of Gd^{3+} substituted Bi$_2$Fe$_4$O$_9$ (BFO) via experimental analysis as well as density functional theory (DFT). Rietveld refined X-ray diffraction data shows phase purity of the samples having orthorhombic phase with space group: "*Pbam*." Gd^{3+} ions substitution at Bi^{3+}-site is confirmed by the shift in peaks ((002) and (220)) at higher 2θ angles as well as the reduction in lattice parameters. The PBE+U calculations predict a band gap of 1.76 eV (BFO) and 1.6 eV (Gd substituted BFO) which is in close agreement with the experimental values. This reduction in band gap due to Gd^{3+} substitution enhances conduction in substituted samples. The calculated density of states illustrates considerable hybridization between Fe-3d and O-2p states with substantial overlap among the Bi-6p and O-2p states. Incorporating Gd^{3+} ions further introduces additional exchange interactions between Gd-Fe$_t$ and Gd-Fe$_o$, thus leading to enhanced magnetization as well as an increase in antiferromagnetic transition temperature (T_N). This characteristic feature is supported by temperature-dependent magnetic susceptibility (χ) and dχ/dT plots. Hence, our experimental and theoretical findings suggest that BFO and its substituted samples are potential multiferroic materials for various device applications.
© 2024 The Electrochemical Society ("ECS"). Published on behalf of ECS by IOP Publishing Limited. All rights, including for text and data mining, AI training, and similar technologies, are reserved. [DOI: 10.1149/2162-8777/ad910d]

Ever since the discovery of the linear magnetoelectric (ME) effect where an electric polarization (magnetisation) is linearly induced by an applied magnetic (electric) field, research in magnetoelectrically coupled multiferroics has seen enormous growth owing to its diversified multifunctional device applications.[1–5] This class of material offers additional degrees of freedom in device designing where magnetic and electric polarization can be tailored, and this could be very subtle to electric and magnetic fields respectively. Nowadays, there is a huge demand to replace the current-based approach with an electric field.[6,7] From this point of view, the fabrication of the "ultimate memory devices" has been an ever-increasing demand owing to their robust, dense, fast, non-volatile, and less energy-expensive features.[8–10] Further, device miniaturization could lead to ultra-low power energy usage with enhanced reading and writing speeds. These objectives can be achieved by using various multiferroic and magnetoelectric materials.[10–13] Despite such remarkable technological applications, the natural occurrence of single-phase ME multiferroics is very rare in nature. This is due to their mutual exclusive characteristics and incompatibility between the order parameters.[1,13] Generally, most of the ME multiferroic systems known so far are functional below the cryogenic temperature. So, exploring new classes of near room temperature ME materials is under intensive focus which could exhibit strong ME coupling at ambient temperature to meet the necessity of practical applications.

Given that, Bi$_2$Fe$_4$O$_9$ (BFO) a material proto-type of Cairo-spin lattice and a well-known antiferromagnetically ordered system has drawn considerable attention in the past few years. BFO shows substantial ME coupling close to room temperature with Néel temperature (T_N) $\sim$ 260 K.[14] Moreover, BFO shows a unique pentagon spin frustration arising due to the competing exchange interactions among different kinds of Fe^{3+} ions, thus leading to a non-collinear magnetic structure eventually generating a peculiar pentagon spin frustration.[15] Over the past few decades, BFO has gathered the considerable attention of researchers and has also been extensively studied for its numerous practical applications such as gas sensors,[16] magnetic,[17] electronic,[18] photo-to-current response,[19] photo-catalytic,[20] etc. However, despite showing near room temperature ME coupling and numerous potential applications, the desire for further improving these novel properties has stimulated the researchers to chemically substitute suitable elements at the Bi^{3+}-site as well as Fe^{3+}-site of BFO.[21–29] Pristine BFO is reported to be a multiband semiconductor or magnetic semiconductor according to various research groups using density functional theory (DFT) calculations.[30,31] Yet, most electronic structure studies yield differing densities of states (DOS) and band structures. Some computational studies have also investigated ferromagnetic BFO.[32] Due to similar ionic radii, rare Earth ions are considered suitable dopants at the Bi-site of BFO. Additionally, the higher saturation magnetization of rare Earth dopants can create additional magnetic exchange interaction paths with Fe ions, thereby increasing the ordering temperature. However, except for a few studies,[33–35] the effect of rare Earth dopants at the Bi-site on various properties of BFO has not been investigated thoroughly.

The objective of this manuscript is to study the effect of structural, electronic, and magnetic properties due to the substitution of a rare Earth element i.e., gadolinium (Gd) at the Bi-site of BFO. It is to be noted that Gd^{3+} is a magnetically active element having an effective magnetic moment of $\sim$8 μ_B as compared to that of Fe^{3+} ions ($\sim$6 μ_B). So, it is apparent that the competing exchange interaction among Gd^{3+} and Fe^{3+} i.e., *f-d* coupling is expected to have a substantial impact on the physical properties of the Gd^{3+} substituted BFO samples. Taking this into consideration, we have tried to investigate the above physical properties using ab initio total-energy calculations supported by experimental study.

Experimental and Computational Details

Sample preparation procedure.—The polycrystalline samples of Bi$_{2(1-x)}$Gd$_{2x}$Fe$_4$O$_9$ (x = 0.01 and 0.02) abbreviated as BGFO1 (x = 0.01) and BGFO2 (x = 0.02) were prepared using high purity oxides (>99.9%, Sigma Aldrich) i.e. Bi$_2$O$_3$, Gd$_2$O$_3$ and Fe$_2$O$_3$ by conventional solid state reaction route. The above raw materials were taken in stoichiometric proportions, mixed thoroughly, grounded for 2 h, and calcined at 800 °C for 12 h followed by a sintering at 850 °C

^{z}E-mail: soumyaranjan.mohapatrafpy@kiit.ac.in

for 10 h.[36] For phase confirmation, the sintered samples were characterized by X-ray diffraction (XRD) measurement, RIGAKU, JAPAN. The room temperature XRD measurements were carried out using Cu-Kα radiation ($\lambda = 1.54$ Å) in a wide range of Bragg angles ($10° \leqslant 2\theta \leqslant 70°$) with a slow scan rate of 3°/min. The magnetization measurements for a wide temperature range of 100–330 K were carried out using a cryogen-free 7 T-SQUID-VSM, Magnetic Property Measurement System (Quantum Design, USA). Finally, the room temperature ferroelectric properties of the samples (P-E loop) were measured on a standard ferroelectric tester using a Radiant Precision Premier II unit.

Computational details.—Density functional theory (DFT) calculations were performed using the Vienna ab initio Simulation Package (VASP),[37] utilizing projector-augmented wave (PAW) potentials.[38] A plane-wave basis set with a kinetic energy cut-off of 600 eV was utilized, alongside Gaussian smearing with a broadening of 0.01 eV. Brillouin zone integration was performed using a Monkhorst–Pack[39] $6 \times 6 \times 8$ **k**-point mesh. Convergence criteria were set to 1×10^{-5} eV for total energy and 0.01 eV/Å for the Hellmann-Feynman force on each atom. The Perdew–Burke–Ernzerhof (PBE)[40] exchange–correlation functional was applied. Additionally, the on-site Coulomb interaction (U) on Fe 3d and Gd 4f orbitals was incorporated using the spherically averaged DFT+U method, with U_{eff} values set at 4.5 eV[41,42] and 6 eV,[43] respectively. Lastly, the electric dipoles of non-collinear and collinear systems were calculated using the Berry phase approach within the modern theory of polarization.[44,45]

Results and Discussion

The phase purity of the synthesized polycrystalline BFO, BGFO1, and BGFO2 are confirmed through Rietveld refinement of room temperature X-ray diffraction (XRD) data as shown in Fig. 1. All the XRD patterns exhibit an orthorhombic phase with space group "*Pbam*." The fitting parameters listed in Table I are in good agreement with previous literature.[28] Due to the substitution of Gd^{3+} ions having lower ionic radius than that of Bi^{3+} ions, a substantial shift of the peaks i.e. (002) and (220) to higher 2θ angles can be seen (inset of Fig. 1) with an increase in Gd^{3+} concentration. As a result, the reduction of lattice parameters as well as cell volume is also evident in Table I.

Moreover, BFO adopts a complex orthorhombic structure as shown in Fig. 2a. The unit cell contains two formula units with two distinct Fe atoms i.e., Fe_o and Fe_t occupying octahedral and tetrahedral positions respectively. The relaxed lattice parameters of BFO are determined as $a = 8.11$ Å, $b = 8.56$ Å, and $c = 6.11$ Å within the PBE-DFT level of theory, closely resembling the experimental values as listed in Table I. It is to be noted that the theoretically calculated value of cell volume i.e., 424.16 Å^3 is slightly higher than the experimental range (403–404 Å^3). This could be ascribed to the presence of defects and vacancies in the synthesized samples. Furthermore, the Fe–O bond distance in octahedral coordination (2.00 Å–2.07 Å) is observed to be comparatively greater than that in tetrahedral coordination (1.85 Å–1.92 Å). This behavior is expected to play a significant role in governing the magnetic and magnetodi-electric properties, which will be discussed subsequently. The presence of both octahedral and tetrahedral coordination in BFO may result in the splitting of the Fe d states into (t_{2g}, e_g) and (t_2, e) for octahedral and tetrahedral coordination, respectively. These states can be filled with $t_{2g}^5(t_2^5)$ and $e_g^0(e^0)$ for a low-spin configuration and $t_{2g}^3(t_2^3)$ and $e_g^2(e^2)$ for a high spin configuration in octahedral (tetragonal) coordination. The calculated magnetic moments at the Fe sites are ~4.3 μ_B, suggesting a high spin state for Fe^{3+} ions at both sites, which aligns with experimental findings.[29] Figure 2b illustrates the spin arrangements in the high spin configuration for both octahedrally and tetrahedrally coordinated Fe ions.
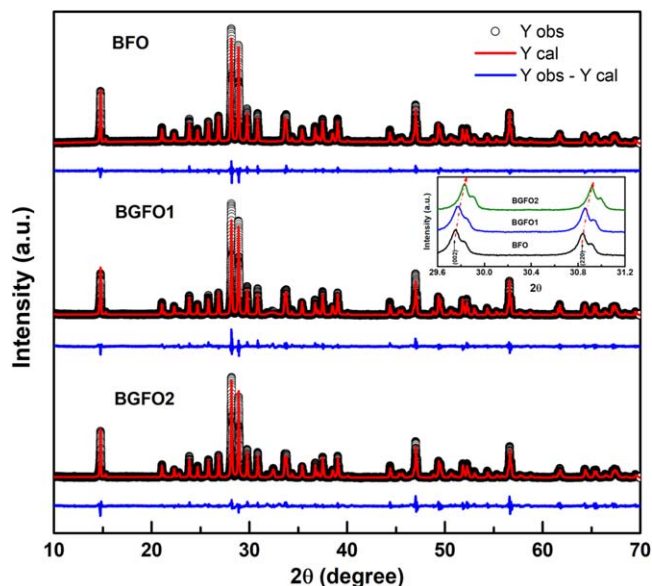

Figure 1. Rietveld refined XRD patterns of BFO, BGFO1 and BGFO2 at room temperature.

Figures 3a–3c depict temperature-dependent DC magnetic susceptibility (χ) measurement of BFO, BGFO1, and BGFO2 under zero field cooled (ZFC) and field cooled warming (FCW) at an applied magnetic field of 1 kOe for a temperature range of 100–330 K. To distinctly trace the T_N of BFO and its substituted samples, we have presented dχ/dT vs temperature plots in the insets of Figs. 3a–3c. Here, we notice that T_N of BFO = 250 K, BGFO1 = 252 K, and BGFO2 = 256 K. The enhancement in T_N can also be attributed to the modification of the Fe_t-O-Fe_t super-exchange interaction in terms of lattice distortion in the unit cell. This relates to our XRD analysis where an increase in Gd^{3+} leads to a decrease in lattice parameters and a reduction in strongly antiferromagnetically coupled Fe_t-O bond lengths. From Figs. 3a–3c, we notice a slight mismatch of ZFC-FCW data in BGFO1 and BGFO2 samples which is completely absent in the ZFC-FCW data of BFO. This irreversibility in ZFC-FCW data below T_N could be an indication of magnetic glassiness behavior in Gd substituted samples unlike strong AFM behavior as seen in the case of BFO. It is to note that, magnetic glassiness behavior could lead to weak FM ordering in BGFO1 and BGFO2. This feature was further confirmed from isothermal magnetization (M-H) plots (not shown here) where for 30 K $\leqslant$ T $\leqslant$ 320 K the Gd substituted sample shows a linear M-H behavior but a non-linear M-H curve for T < 30 K is seen inferring weak FM ordering.[36] Overall, it is evident that the magnetization has increased substantially due to Gd^{3+} substitution and the viable reason could be due to the presence of Fe^{3+} and Gd^{3+} sublattices having their temperature-dependent magnetizations. Additionally, due to uncompensated spins in the two sub-lattices, it is quite obvious that there will be a net magnetic moment in the material. Gd^{3+} has a larger effective magnetic moment (~8 μ_B) than Fe^{3+} ions (~5.9 μ_B) and often prefers to order ferromagnetically at low temperatures. Hence, the coupling between Gd^{3+} and Fe^{3+} ions (*f-d* coupling) is a possible reason for enhanced magnetic behavior. Moreover, incorporating Gd^{3+} ions introduces additional interactions between tetrahedral and octahedral coordinated Fe ions with Gd ions thereby strengthening the exchange interaction and potentially leading to an increase in the transition temperature (T_N). Furthermore, the substitution at the Bi^{3+} sites results in a decrease in lattice parameters due to the smaller size of Gd^{3+}, causing a reduction in the strongly antiferromagnetically coupled Fe–O bond lengths. This change modifies the Fe–O–Fe super-exchange interaction in terms of lattice distortion in the unit cell, thereby enhancing T_N, which is evident from our experimentally measured temperature-dependent susceptibility data.

Table I. Variations of lattice parameters (obtained from the Rietveld refinement of XRD data) and ferroelectric properties (P-E loop) of BFO, BGFO1, and BGFO2.

Samples	Lattice parameters					Ferroelectric properties	
	a (Å)	b (Å)	c (Å)	Volume (Å^3)	χ^2	$2P_r$ ($\mu C/cm^2$)	$2E_c$ (kV/cm)
BFO	7.9735(2)	8.4414(4)	6.0027(5)	404.027(4)	3.66	0.292	15.55
BGFO1	7.9727(9)	8.4411(3)	6.0023(9)	403.958(8)	2.71	0.162	8.92
BGFO2	7.9673(4)	8.4349(2)	5.9997(8)	403.211(5)	3.06	0.016	1.11
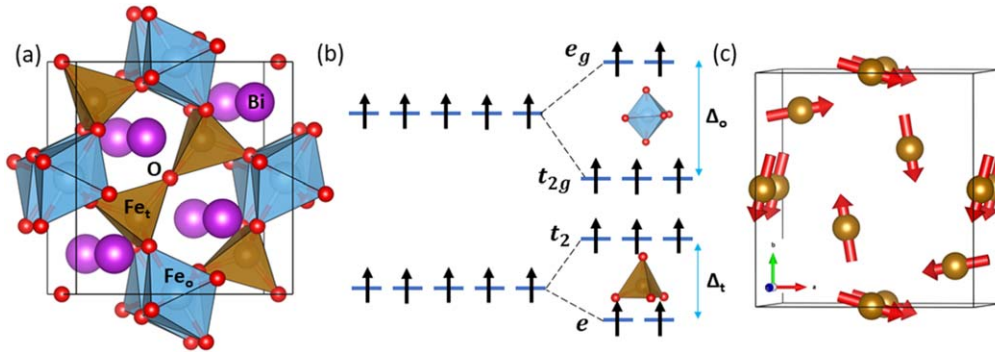
Figure 2. Crystal structure of BFO: (a) The crystal structure of BFO showcases arrangements of Fe–O polyhedra in both tetrahedral and octahedral configurations. (b) Crystal field splitting of Fe d states in the high spin configuration is depicted for both geometries. (c) The non-collinear magnetic structure of BFO (only Fe atoms are shown for simplicity).
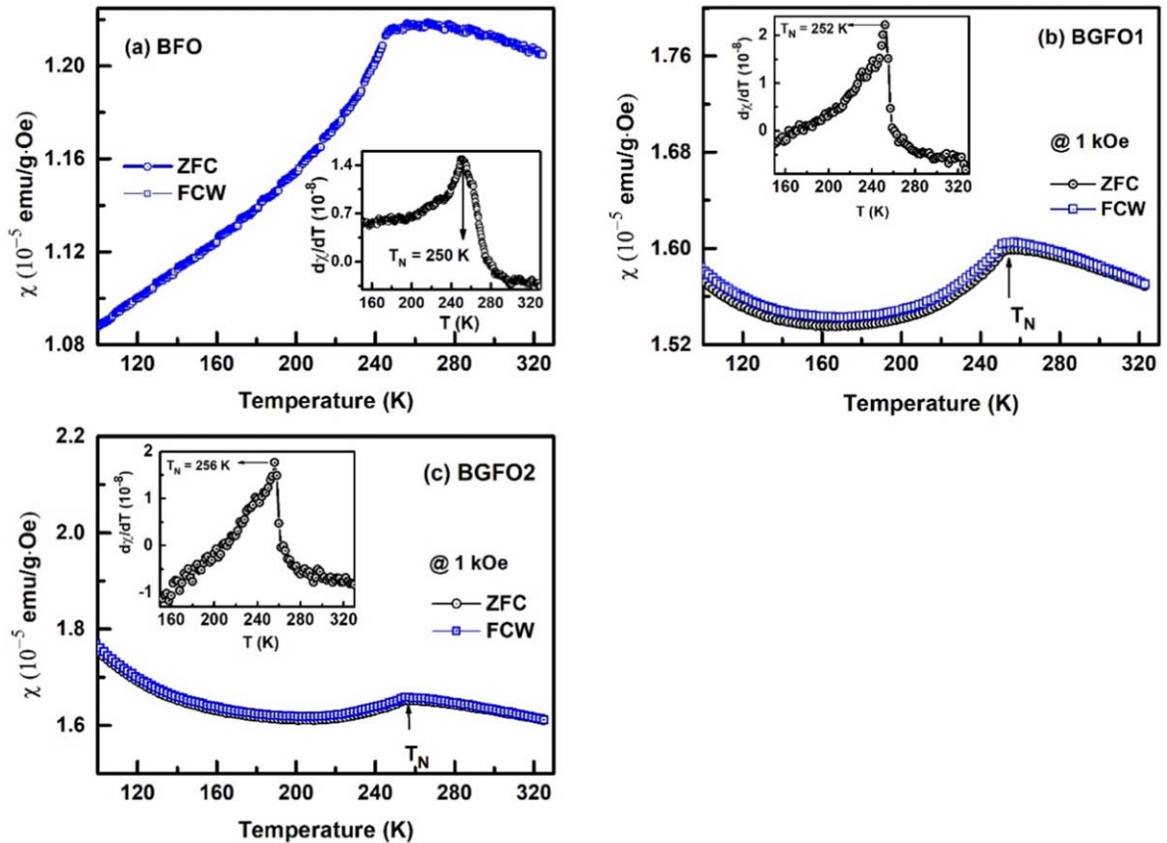
Figure 3. (a)–(c) χ-T plot of BFO, BGFO1 and BGFO2 under 1 kOe. Insets show dχ/dT vs T plots distinctly revealing the AFM transition temperature (T_N).

Next, using the density functional theory-based calculations, we have analysed the electronic and magnetic structure of BFO and Gd substituted BFO configurations. Figure 5 shows the total density of states for (a) antiferromagnetic (AFM) and (b) ferromagnetic (FM) configurations. The AFM configuration considered here as depicted in Fig. 2c follows the non-collinear AFM model as proposed by
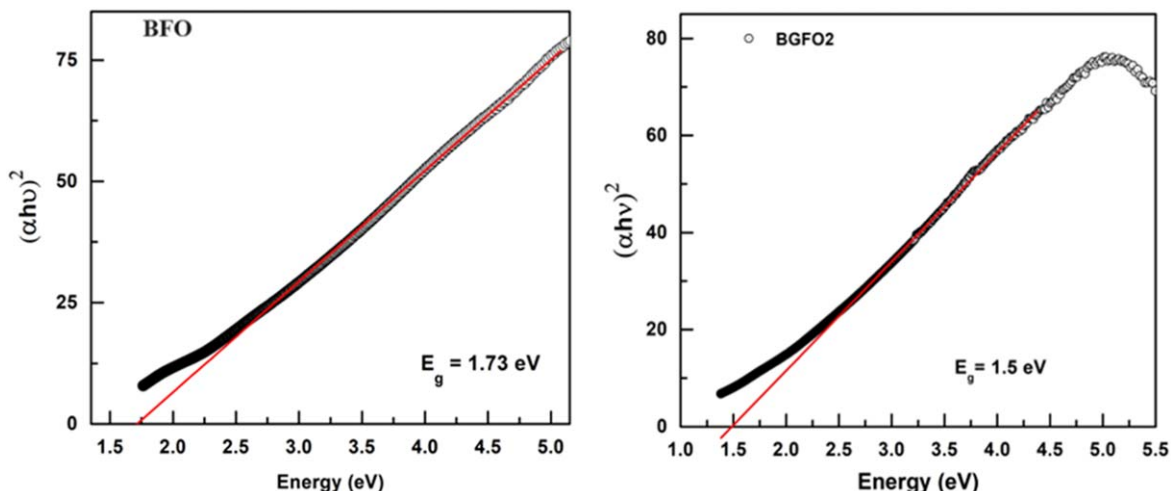
Figure 4. $(\alpha h\upsilon)^2$ vs energy (eV) plot displaying the energy band gap of (a) BFO and (b) BGFO2.
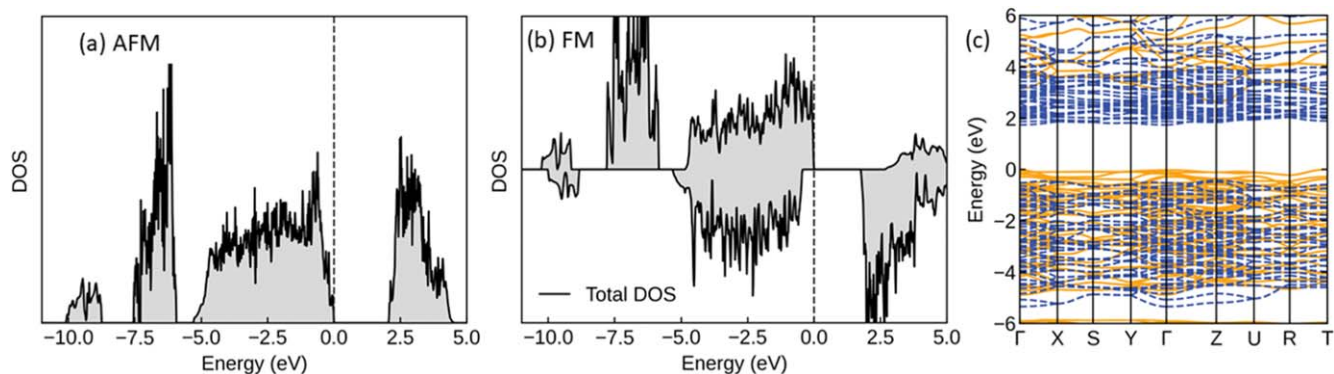

Figure 5. The total density of states of BFO in (a) AFM and (b) FM configurations. The electronic band structure of the FM configuration is given in (c). The orange (solid) and blue (dashed) lines represent the majority and minority spin channels respectively.
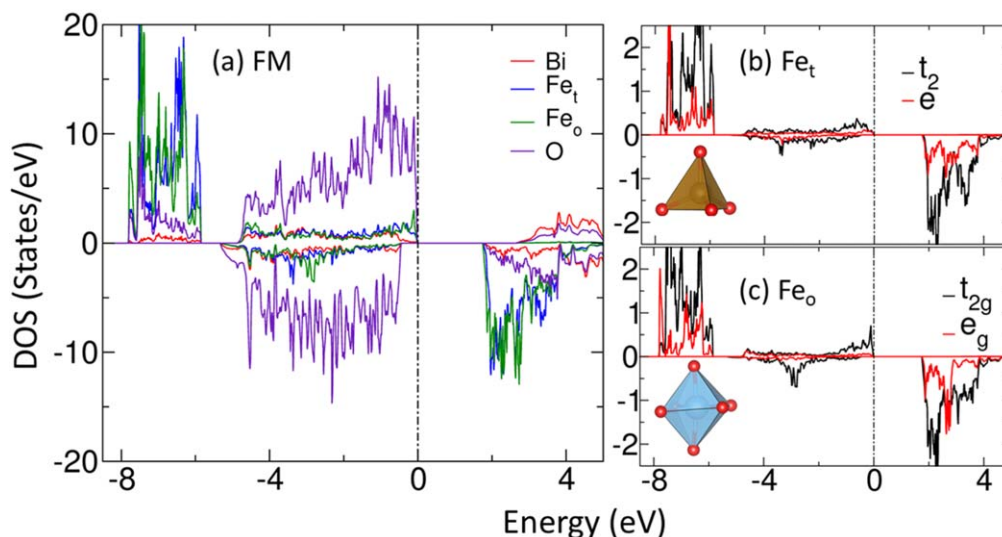

Figure 6. Projected electronic structure: (a) spin-polarized atom-projected DOS of BFO in the FM configuration. The orbital projected DOS in the (b) tetrahedral and (c) octahedral coordinated Fe ions.

Ressouche et al.[15] In a non-collinear AFM configuration, the magnetic moments of the Fe ions are not aligned opposite to each other, rather the moments are canted, resulting in a complex magnetic structure where the moments form a non-linear arrangement. Such non-collinear configuration can result in exciting properties like weak ferromagnetism or magnetoelectric effects due to the spin-canting. Unlike the non-magnetic configuration, which demonstrates metallic behavior, the AFM (Fig. 5a) and FM (Figs. 5b, 5c) states exhibit band gaps. This is attributed to the exchange splitting introduced by incorporating spin polarization into
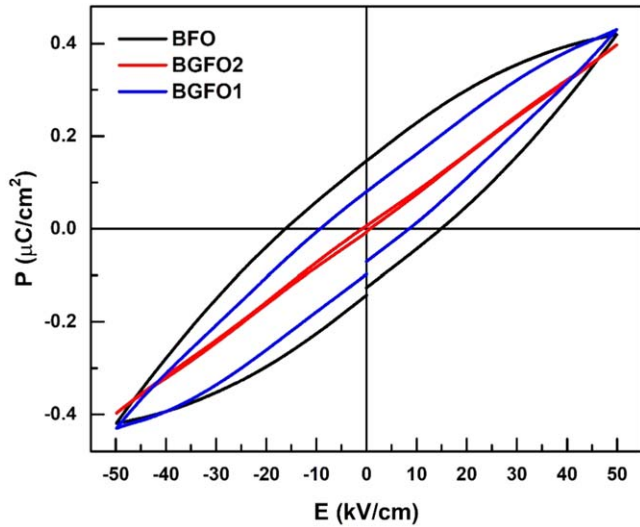
Figure 7. Room temperature P–E hysteresis loop of BFO, BGFO1 and BGFO2 samples.

the calculations. The significant exchange splitting between the majority and minority spin bands along with the crystal field splitting of Fe-3d orbitals are key features of the electronic structure of $Bi_2Fe_4O_9$.[32] The calculated bandgaps within the PBE+U level of theory are 2.05 eV and 1.76 eV respectively. Notably, the calculated bandgap for the FM configuration closely aligns with our experimental observations as shown in Fig. 4.[46] The optical band gap energy (E_g) was experimentally calculated using Wood and Tauc's relation[47] i.e. $\alpha h\upsilon = A(h\upsilon - E_g)^n$, where, α is the optical absorption coefficient, $h\upsilon$ is the energy (in eV), A is the constant (independent of photon energy), E_g is the optical band gap and n is a constant associated with different types of electronic transitions i.e. $n = 1/2$, 2, 3/2 or 3 for direct allowed, indirect allowed, direct forbidden and indirect forbidden transitions respectively. In our case, $n = 1/2$ is used in the above equation which suggests a direct allowed transition. Linear fitting to the experimental data in Figs. 4a, 4b is done and later extrapolated to obtain $E_g = 1.73$ eV for BFO and 1.5 eV for BGFO2.

To have a detailed understanding of the electronic structure, we have plotted the partial DOS for BFO as given in Fig. 6. The valence band spanning up to -5 eV from the fermi level (E_F) primarily consists of Fe 3d–O 2p states, resulting in a magnetic moment at the O sites ($\sim0.2\,\mu_B$) due to this hybridization. The half-filled Fe d states contribute predominantly to the DOS in the range of -6 to -8 eV. Additionally, Bi 6p lone pair states are noticeable approximately

10 eV below the E_F. Similarly, the top of the conduction band is primarily composed of unoccupied Fe 3d bands, with significant contributions from O and Bi states, as illustrated in Fig. 6a. Figures 6b and 6c display the orbital decomposed DOS for Fe$_t$ and Fe$_o$ in the FM configuration of BFO, respectively. It is clear that the majority of spin channels of both t_2 and e in Fe$_t$ and t_{2g} and e_g in Fe$_o$, are fully occupied. Notably, the crystal field splitting between t_2 and e (~0.03 eV) in Fe$_t$ is considerably higher than that between t_{2g} and e_g (~0.01 eV) in Fe$_o$. This disparity could be ascribed to the shorter bond distance of Fe$_t$–O compared to Fe$_o$–O, which might induce greater repulsion in the tetrahedral coordination than in the octahedral coordination. However, despite this difference, the crystal field splitting remains lower compared to the exchange energy, potentially leading to high spin states of Fe^{3+}, consistent with our experimental observations.[29] In context to this, the presence of Bi^{3+} lone pair and O-2p can be considered as a responsible factor for ferroelectric properties in the samples. Also, in the case of BFO, it has been reported that a lone s^2 pair of electrons in Bi^{3+} ions hybridize with the 2p orbital of O^{2-} ions, thus forming a localised lobe causing ferroelectricity.[48] So, in order to understand the ferroelectric hysteresis behaviour of the Gd-substituted samples, room temperature polarization vs electric field (P-E loop) study of BGFO1 and BGFO2 is shown in Fig. 7 and is compared with BFO. No saturation in the hysteresis curve is seen in all the samples up to a maximum applied electric field of ±50 kV cm^{-1}, which indicates the partial reversal of the polarization. A slim P-E loop with a decrease in remnant polarization ($2P_r$) and coercive field ($2E_c$) is observed with an increase in Gd-substitution, implying a significant effect of the substitution on the ferroelectric property of the system. The experimental values of $2P_r$ and $2E_c$ are listed in Table I. Moreover, we have calculated the spontaneous polarization by comparing the polar (non-collinear magnetic) structure with the non-polar reference structure (collinear phase) using the Berry phase approach. The estimated value is approximately 0.2 μC cm^{-2}, which is in reasonable agreement with our experimental result (shown in Table I) and other reported values.[48] The non-collinear configuration of BFO can become more complex with the substitution of an additional magnetic element, such as Gd. Consequently, we have not estimated the polarization values for Gd-BFO systems theoretically, which could be a promising direction for our future work.

Additionally, the Gd^{3+} substituted BFO (Gd-BFO) is simulated by substituting one Bi atom with Gd in the unit cell. Owing to the complexity of modelling the non-collinear magnetic structure for Gd-doped BFO, we have examined the electronic properties of the FM phase only and compared it with the FM configuration of pure BFO, as depicted in Fig. 8. The Gd f states are localized approximately 7 eV below the E_F in the valence band, closely positioned to the Fe d states. However, the vacant Gd states reside farther from the E_F in the conduction band compared to the Fe states.
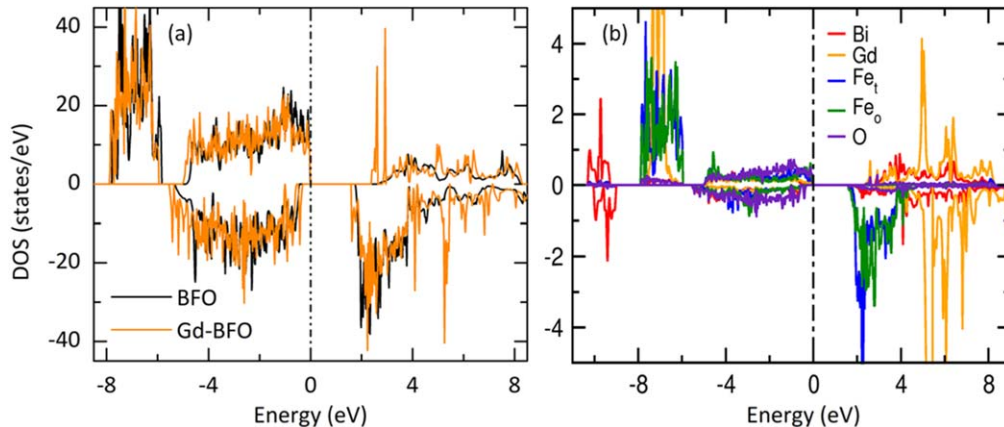

Figure 8. Electronic structure of Gd-BFO: (a) Total DOS for both BFO and Gd-BFO and (b) atom projected DOS for Gd-BFO in the FM configurations. The narrowing of the bandgap is apparent in (a).

The calculated theoretical bandgap reduces to 1.6 eV upon Gd substitution, aligning with experimental (shown in Fig. 4b) and theoretical findings.[49] The reduction in the band gap enhances conduction in Gd-BFO and is primarily attributed to the introduction of Gd^{3+} substitution. This introduction likely decreases the electronic correlation energy associated with the valence state of Fe^{3+} ions.

Conclusions

To summarize, we have successfully synthesized polycrystalline $Bi_{2(1-x)}Gd_{2x}Fe_4O_9$ (x = 0.01 and 0.02) by conventional solid-state reaction technique without any traces of secondary phases. Phase impurity of the sample and its orthorhombic phase was confirmed from room temperature Rietveld refinement of the XRD data. XRD analysis confirmed the substitution of lower ionic radii Gd^{3+} ions at the Bi^{3+}-site by observing a decrease in lattice parameters and shift of peaks (002) and (220) to higher 2θ angles. Crystal field splitting of Fe-d states into (t_{2g}, e_g) and (t_2, e) for octahedral and tetrahedral coordination respectively of BFO was observed. Further, we have used DFT to investigate the electronic and magnetic properties of BFO and its substituted samples. The theoretical calculated values of bandgap within PBE+U theory closely match the experimental values. From the temperature-dependent magnetization study within the temperature range of 100–300 K, a substantial increase in AFM transition temperature (T_N) was noticed i.e., 250 K for BFO to 256 K for BGFO2. This feature is supported by dχ/dT plots for all the samples thereby showing sharp transitions (T_N). Here, Gd^{3+} ions have a larger effective magnetic moment of ~ 8 μ_B as compared to Fe^{3+} ions (~ 5.9 μ_B) along with mutual coupling among Gd^{3+}-Fe^{3+} ions i.e., f-d coupling played a crucial role in enhanced magnetization in Gd-substituted samples. Hence, all these results indicate that the synthesized samples can be a potential candidate for numerous multifunctional device applications.

Acknowledgments

ORCID

S. R. Mohapatra https://orcid.org/0000-0003-3684-9463
Hari S. Mohanty https://orcid.org/0000-0002-1230-156X

References

1. W. Erenstein, N. D. Mathur, and J. F. Scott, *Nature*, **442**, 759 (2006).
2. X. Liang, H. Chen, and N. X. Sun, *APL Mater.*, **9**, 041114 (2021).
3. J. L. Chung Ming Leung, D. Viehland, and X. Zhuang, , *J. Phys. D: Appl. Phys.*, **51**, 263002 (2018).
4. N. A. Spaldin, S-W. Cheong, and R. Ramesh, *Phys. Today*, **63**, 38 (2010).
5. H. J. Zhao, W. Ren, Y. Yang, J. I. Niguez, X. Ming Chen, and L. Bellaiche, *Nat. Commun.*, **5**, 4021 (2014).
6. T. Taniyama, *J. Phys. Condens. Matter*, **27**, 504001 (2015).
7. M. Liu and N. X. Sun, *Philos. Trans. R. Soc. A*, **372**, 20120439 (2014).
8. J. F. Scott, *Nat. Mater.*, **6**, 256 (2007).
9. T. Kimura, T. Goto, H. Shintani, K. Ishizaka, T. Arima, and Y. Tokura, *Nature*, **426**, 55 (2003).
10. Z. Zhang, Z. Wang, T. Shi, C. Bi, F. Rao, Y. Cai, Q. Liu, H. Wu, and P. Zhou, *InfoMat.*, **2**, 261 (2020).
11. S. Fusil, V. Garcia, A. Barthélémy, and M. Bibes, *Annu. Rev. Mater. Res.*, **44**, 91 (2014).
12. C. Song, B. Cui, F. Li, X. Zhou, and F. Pan, *Prog. Mater Sci.*, **87**, 33 (2017).
13. M. Mostovoy, *npj Spintronics*, **2**, 18 (2024).
14. A. K. Singh et al., *Mater. Res. Express*, **6**, 066107 (2019).
15. E. Ressouche, V. Simonet, B. Canals, M. Gospodinov, and V. Skumryev, *Phys. Rev. Lett.*, **103**, 267204 (2009).
16. A. Poghossian, H. Abovian, P. Avakian, S. Mkrtchian, and V. Haroutunian, *Sensors Actuators B*, **4**, 545 (1991).
17. N. Shamir, E. Gurewitz, and H. Shaked, *Acta Crystallographica section A: Crystal Physics, Diffraction, Theoretical and General Crystallography*, **34**, 662 (1978).
18. Y. Y. Liang, J. X. Lei, X. X. Wang, L. G. Wang, and C. M. Zhu, *J. Mater. Sci.: Mater. Electron.*, **30**, 1691 (2019).
19. Y. Li, Y. Zhang, W. Ye, J. Yu, C. Lu, and L. Xia, *New J. Chem.*, **36**, 1297 (2012).
20. M. Zhang, H. Yang, T. Xian, Z. Wei, J. Jiang, Y. Feng, and X. Liu, *J. Alloys Compd.*, **509**, 809 (2011).
21. A. Glinskaya, G. Petrov, I. Vialikanava, and V. Romanovski, *Chemistry Select*, **8**, e202204285 (2023).
22. C. M. Raghavan, J. W. Kim, J. Y. Choi, J-W. Kim, and S. S. Kim, *Ceram. Int.*, **40**, 14165 (2014).
23. H. Kuzhandaivel, Y. Selvaraj, M. C. Franklin, S. Manickama, and K. S. Nallathambi, *New J. Chem.*, **45**, 15223 (2021).
24. R. R. Awasthi, S. K. Trivedi, V. S. Chandel, M. Shariq, H. J. Alathlawi, and S. P. Singh, *ACS Omega*, **8**, 15960 (2023).
25. Y. Qiu, Z. J. Zou, R. R. Sang, H. Wang, D. Xue, Z. M. Tian, G. S. Gong, and S. L. Yuan, *J. Mater. Sci.: Mater. Electron.*, **26**, 1732 (2015).
26. M. Rozova, V. Grigoriev, I. Bobrikov, D. Filimonov, K. Zakharov, O. Volkova, A. Vasiliev, E. Antipov, A. Tsirlin, and A. Abakumov, *Dalton Trans.*, **45**, 1192 (2016).
27. S. R. Mohapatra, S. D. Kaushik, and A. K. Singh, *Mater. Res. Express*, **5**, 016107 (2018).
28. S. R. Mohapatra, P. N. Vishwakarma, S. D. Kaushik, and A. K. Singh, *J. Appl. Phys.*, **122**, 134103 (2017).
29. S. R. Mohapatra, P. N. Vishwakarma, S. D. Kaushik, R. J. Choudhary, N. Mohapatra, and A. K. Singh, *J. Appl. Phys.*, **121**, 124101 (2017).
30. Y. Zhang, Y. Guo, H. Duan, H. Li, L. Yang, P. Wang, C. Sun, B. Xu, and H. Liu, *RSC Adv.*, **4**, 28209 (2014).
31. S. Sun, W. Wang, L. Zhang, and M. Shang, *J. Phys. Chem. C*, **113**, 12826 (2009).
32. S. H. Zainab Irshad, M. A. Shah, M. M. Rafiq, and J. Hasan, *Alloys Compd.*, **624**, 131 (2015).
33. K. Subha Rao, S. Manjunath Kamath, R. Rajesh Kumar, G. Kavitha, E. MeherAbhinav, S. Sobana Shri, S. Induja, and C. Gopalakrishnan, *Mater. Lett.*, **297**, 129960 (2021).
34. S. K. Rao, B. Renganathan, A. Kalai Priya, R. Rajesh Kumar, R. Jothi Ramalingam, M. R. Kumar, R. Kesavasamy, G. M. Ramanujam, and M. S. Kamath, *Ceram. Int.*, **50**, 13993 (2024).
35. S. Krishna Rao, E. Meher Abhinav, D. Jaison, A. Sundararaj, M. Santhiya, R. Althaf, and C. Gopalakrishnan, *Vacuum*, **172**, 109109 (2020).
36. S. R. Mohapatra, A. Swain, C. S. Yadav, S. D. Kaushik, and A. K. Singh, *RSC Adv.*, **6**, 112282 (2016).
37. G. Kresse and J. Furthmüller, *Phys. Rev. B*, **54**, 11169 (1996).
38. P. E. Blöchl, *Phys. Rev. B*, **50**, 17953 (1994).
39. J. D. Pack and H. J. Monkhorst, *Phys. Rev. B*, **16**, 1748 (1977).
40. J. P. Perdew, K. Burke, and M. Ernzerhof, *Phys. Rev. Lett.*, **77**, 3865 (1996).
41. S. Ameer, K. Jindal, M. Tomar, P. K. Jha, and V. Gupta, *J. Magn. Magn. Mater.*, **475**, 695 (2019).
42. K. Jindal, S. Ameer, M. Tomar, P. K. Jha, and V. Gupta, *Mater. Today Proc.*, **47**, 1637 (2021).
43. L. Patra and B. Liao, *Phys. Rev. Lett.*, **131**, 66703 (2023).
44. R. D. King-Smith and D. Vanderbilt, *Phys. Rev. B*, **47**, 1651 (1993), (R).
45. R. Resta and R. Mod, *Phys.*, **66**, 899 (1994).
46. X. Yuan, L. Shi, J. Zhao, S. Zhou, and J. Guo, *Scr. Mater.*, **146**, 55 (2018).
47. D. L. Wood and J. Tauc, "Weak absorption tails in amorphous semiconductors." *Phys. Rev. B*, **5**, 3144 (1972).
48. Z. M. Tian, Y. Qiu, S. L. Yuan, M. S. Wu, S. X. Huo, and H. N. Duan, *J. Appl. Phys.*, **108**, 064110 (2010).
49. S. K. Rao, A. Kalai Priya, S. Manjunath Kamath, E. Meher Abhinav, B. Renganathan, K. Jeyadheepan, and C. Gopalakrishnan, *Mater. Chem. Phys.*, **278**, 125646 (2022).